Sensors and Materials, Vol. 38, No. 2 (2026) 801–817
MYU Tokyo

S & M 4349

Sensor Physics Data Hybrid-driven Regional Integrated Energy Systems Operation Optimization Considering Dynamic Reliability Assessment and Risk Mapping Framework with High Renewable Energy Penetration

Zai-He Yang,[1] Shi-Hao Yin,[1] Bin Zhang,[1,2*] Ming-Liang Yang,[1] and Jin-Qiu Li[1]

[1]Yunnan Power Dispatching and Control Center, Kunming, Yunnan Province 650500, China
[2]Faculty of Land and Resources Engineering, Kunming University of Science and Technology, Kunming 650093, China

(Received August 2, 2025; accepted October 1, 2025)

Keywords: regional integrated energy systems, physics data hybrid-driven dynamic reliability assessment, reliability assessment, gas turbine fault analysis

The integration of high-penetration renewable energy is significant for environmental improvement and the transformation and upgrading of energy systems. However, the uncertainty of renewable energy generation and component failures pose significant challenges to system stability. In this study, we focus on the optimal scheduling and reliability assessment of regional integrated energy systems (RIESs), and we propose a sensor physics data hybrid-driven dynamic reliability assessment and risk mapping framework for power systems with high renewable energy penetration. The proposed framework integrates quantitative reliability assessment and an uncertainty mapping strategy for high-penetration renewable energy systems, as well as a sensor physics data hybrid-driven dynamic fault rate perception strategy. This enables the precise assessment of system reliability and real-time monitoring and the dynamic perception of component failure risks. When gas turbines fail, the operating costs of integrated energy systems (IESs) rise significantly. For example, the cost of IES1 surges from 16791.27$ to 33299.5$. After equipment recovery, IES1's energy procurement cost decreases by approximately 8.5%, highlighting the value of the proposed framework and algorithm in enhancing the operational efficiency, economy, and reliability of RIESs. In this work, we provide new insights for the optimized design and operational management of IESs.

1. Introduction

Global emission reduction targets are driving the transition to renewable-energy-dominated power systems. However, there is still a lack of standards for operational reliability assessment.(1) Considering that the uncertainty of renewable energy (RE) generation can cause changes in reliability indices,(2) it is necessary to use sensors to detect data in real time and employ

*Corresponding author: e-mail: zhangbin_ynpd@126.com
https://doi.org/10.18494/SAM5872

ISSN 0914-4935

scientifically sound analysis methods to consider various factors to establish a comprehensive framework for evaluating stability, resilience, and economics.[3]

Current studies employ data-driven techniques and storage coordination to enhance high-RE system efficiency, while a parallel stream optimizes electric vehicle (EV) technologies and user behavior for supply–demand balance. To begin with, Kanno adopted generative adversarial networks (GANs) to capture RE spatiotemporal patterns, thereby cutting costs and raising penetration;[4] nevertheless, GANs face heavy computation in high dimensions. Building on this, Ghanbarzadeh *et al.* confirmed that storage mitigates RE intermittency, yet the authors omitted the impacts of extreme events and unit failures on capacity planning.[5] In contrast to these supply-side efforts, Lee *et al.* demonstrated that merely 4.5–15.3% EV vehicle-to-grid (VZG) participation can save 36.5–45.6% storage and 3.35% cost;[6] however, the authors neglected hydrogen and carbon trading. Addressing this gap, Li *et al.* coupled EVs, hydrogen vehicles, and a carbon mechanism, achieving an extra 0.4% CO_2 reduction,[7] although it still relies solely on time-of-use pricing. Subsequently, Motlagh *et al.* introduced distribution locational marginal pricing to heighten grid flexibility for RE, but offered no concrete optimization data.[8] From the findings of Motlagh *et al.*, Rehman *et al.* merged renewable energy-integrated battery charging system with ultrafast charging, cutting costs by ~40% and emissions by 65.2%.[9] Moreover, Sica *et al.* validated dynamic-pricing acceptance via a discrete-choice model, yet overlooked RE uncertainty.[10] Finally, Shariatzadeh *et al.* enriched the picture by showing that social norms and risk perception inject further demand-side uncertainty, thereby complementing the supply-side focus of earlier works.[11] In summary, while the literature has advanced along multiple fronts, the reliable quantification of system reliability and user-driven uncertainties remains limited.

Reliability studies on high-RE integrated systems have migrated from single grids to multi-energy coupling, now embedding user loads and maintenance. First, Wang *et al.* proposed a four-stage rapid method that cuts RTS error to 3.7%, yet it scales poorly.[12] To tackle large grids, Niu *et al.* modeled cascading failures and shrank computation by 98% with <6% error; however, they omitted RE/storage faults.[13] On the other hand, van Nooten *et al.* adopted graph isomorphism for medium-voltage fault reliability, but they stayed within one grid.[14] Bridging this gap, Baik *et al.* coupled outage and photovoltaic (PV) -storage simulators, yet neglected maintenance impacts.[15] Consequently, Shariatzadeh *et al.* introduced an extended virtual age model to tune maintenance and curb faults.[16] Building on post-fault stability, Lu *et al.* rebalanced loads via price signals, although only indirectly.[17] Thereafter, Liu *et al.* showed that coordinated EV-electrical energy storage charging cuts cost under EV faults and speed recovery, yet lacks EV–equipment coordination.[18] Complementarily, Yang *et al.* quantified EV uncertainty, trimmed storage by ~20% and overload risk, but offered no fault scheme.[19] Subsequently, Agarwal and Sharma employed V2G to reshape post-fault profiles.[20] Extending to protection, Cao *et al.* co-optimized generators and relays, lifting reliability from 0.7717 to 0.9077, although for non-repairable grids.[21] Advancing further, Shabanian-Poodeh *et al.* embedded electricity–gas coupling via stochastic optimization, boosting reliability by 12.53% and cutting cost by 2.81%, yet skipped parameter sensitivity.[22] Finally, Liu *et al.* closed the loop with energy-hub + self-adaptive particle swarm optimization, cutting the annual cost by 15.2% and realizing a 50.08% parameter impact.[23] Overall, static models still lack real-time dynamics.

In-depth regional integrated energy system (RIES) research still confronts unresolved reliability issues under high renewable penetration. First, numerous studies have succeeded in enhancing the economic efficiency and flexibility of systems. However, they often lack robust quantitative metrics for evaluating system reliability, as well as an explicit method for mapping uncertainties under high RE penetration. Second, current assessments rely on static models to evaluate single-component failures. These models are probabilistic in nature. Consequently, they cannot capture the dynamic evolution of component fault risk. Third, the optimization algorithms for RIES scheduling frequently fall into local optima. Moreover, they suffer from low population diversity, which collectively limits their effectiveness in solving large-scale, multi-objective problems.

To address these gaps, in this paper, we propose a physics-data hybrid dynamic reliability and risk-mapping framework for highly renewable power systems. This framework is supported by an enhanced multi-objective gray wolf optimizer (MGWO) algorithm, which is designed to boost the efficiency and economics of RIES. Its contributions are as follows:

- a hybrid framework that quantifies reliability and maps uncertainty under high RE penetration by integrating renewable variability with sensor-driven dynamic fault-rate perception,
- a concise reliability metric—daily reliable renewable capacity and power deficit rate—that quantifies RE integration impacts, guiding stable, efficient operation, and
- a hybrid fault-rate model merging physics-based degradation with sensor-detected real-time data to create state-sensitive, time-varying failure rates, superseding static probabilities.

This paper proceeds as follows. In Sect. 2, we build the RIES-based model and the hybrid physics data reliability/risk framework. In Sect. 3, we upgrade the multi-objective MGWO. In Sect. 4, we present the bi-level RIES scheduling process, and in Sect. 5, we verify the framework and algorithm via case studies.

2. Formulation of Sensor Physics Data Hybrid-driven Collaborative Optimization Framework for RIES

The RIES integrates renewables with conventional equipment, featuring electricity-heat-cooling networks and self-balancing capabilities. It operates via a bi-level structure: the upper level involves distributed energy units, dynamic pricing operators, and grid companies, whereas the lower level consists of zones with diverse load characteristics. Figure 1 shows the optimization framework of the RIES, and Fig. 2 shows the sensor schematic diagram.

2.1 Constraints and operational optimization objective functions for RIES

Equipment modeling and constraints in RIES are discussed in Ref. 24. The multi-objective function of the energy producer in matrix form is as follows.

$$M_{EP} = \max \begin{bmatrix} \varepsilon_1 M_{run} \\ \varepsilon_2 M_{sell} \end{bmatrix} \tag{1}$$

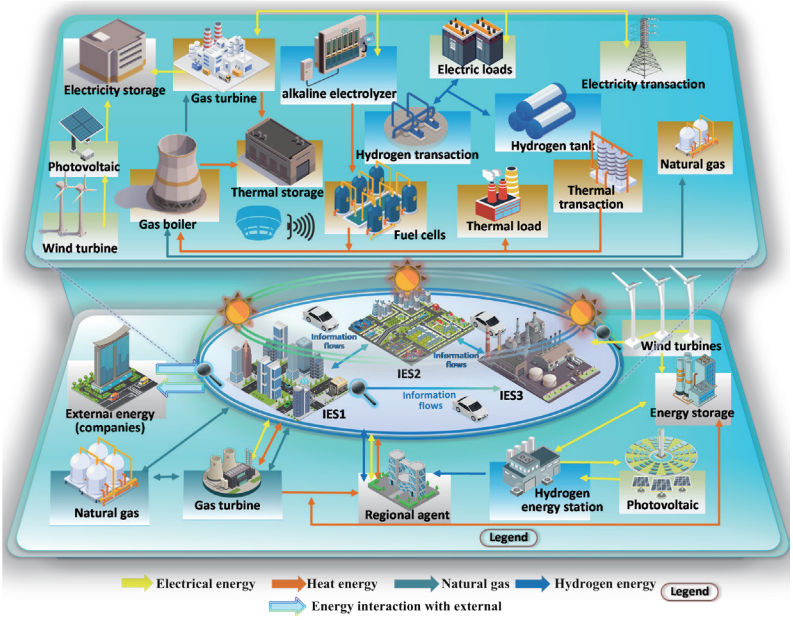

Fig. 1. (Color online) Optimization framework of RIES.

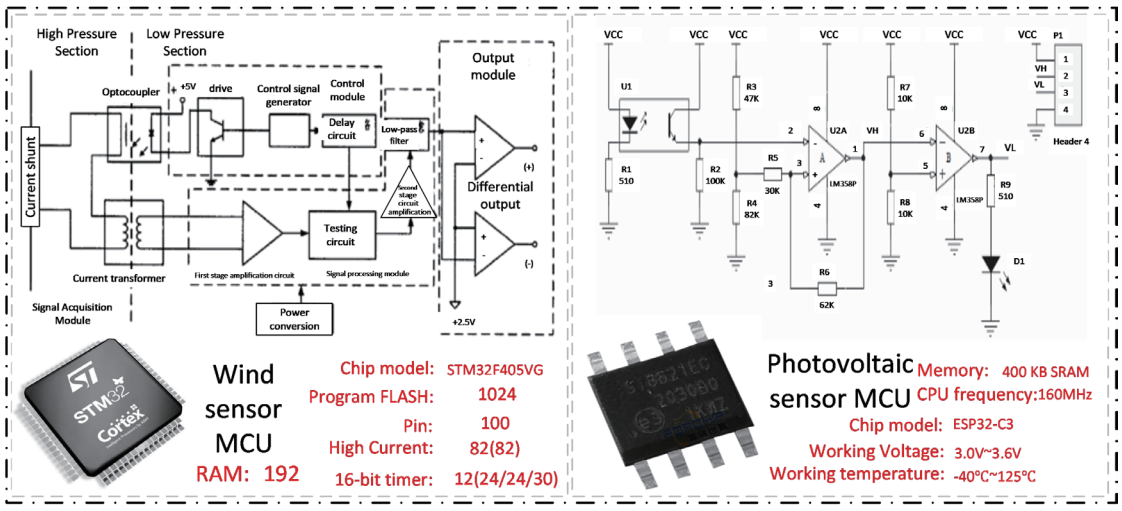

Fig. 2. (Color online) Sensor schematic diagram.

$$\begin{cases} M_{sell} = \sum_{t=1}^{T}\left[m_{t,buy}^{e} E_{t,sell}^{e} + m_{t,buy}^{h} E_{t,sell}^{h} + m_{t,buy}^{g} E_{t,sell}^{g} \right] \\ M_{run} = \sum_{t=1}^{T}\left[m_{t,om} + m_{t,p} + m_{t,gas} \right] \end{cases} \tag{2}$$

The mathematical expression of the energy manager's objective function is as follows.

$$M_{EO} = \max\begin{bmatrix} M_{sell}^{e} & M_{buy}^{e} \\ 1 & 1 \end{bmatrix} \tag{3}$$

$$\begin{cases} M_{sell}^{e} = \sum_{t=1}^{T}\left\{E_{t,sell}^{EP} e_{t,sell} + H_{t,sell}^{EP} h_{t,sell}\right\} \\ M_{buy}^{e} = \sum_{t=1}^{T}\left\{E_{t,buy}^{EP} e_{t,buy} + H_{t,buy}^{EP} h_{t,buy}\right\} \end{cases} \tag{4}$$

$$\begin{cases} E_{t,sell}^{EP} = E_{t,buy}^{IES-1} + E_{t,buy}^{IES-2} + E_{t,buy}^{IES-3} \\ H_{t,sell}^{EP} = H_{t,buy}^{IES-1} + H_{t,buy}^{IES-2} + H_{t,buy}^{IES-3} \end{cases} \tag{5}$$

2.2 Sensor physics data hybrid-driven dynamic reliability assessment and risk mapping framework for power systems with high RE penetration

The sensor physics data hybrid-driven dynamic reliability assessment and risk mapping framework for power systems with high RE penetration mainly includes two strategies: (1) quantitative reliability assessment and uncertainty mapping strategy for high-penetration RE systems, and (2) sensor physics data hybrid-driven dynamic fault rate perception.

2.2.1 Quantitative reliability assessment and uncertainty mapping strategy for high-penetration RE systems

This strategy quantitatively assesses system reliability under high RE penetration. As the renewable output proportion rises, its uncertainty significantly affects reliability metrics. A higher output uncertainty lowers system reliability. Key indicators include the daily average reliable renewable generation capacity and energy deficit rate. The mapping of uncertainty factors includes the quantification of RE output uncertainty and the output correlation coefficient of regional RE.

The calculation formula for the daily average reliable renewable generation capacity is as follows.

$$\eta = \frac{\sum_{t=1}^{24} P_{t,pv}^{IES} + \sum_{t=1}^{24} P_{t,wt}^{IES}}{\sum_{t=1}^{24} P_{t,pv}^{IES} + \sum_{t=1}^{24} P_{t,wt}^{IES} + \sum_{t=1}^{24} P_{t,else}^{IES}} \times 100\% \tag{6}$$

The energy deficit rate is primarily used to assess the impact of power shortfalls within the system. It is defined as the ratio of the power deficit to the total system load. Since the system

load forecast is fixed, a higher energy deficit rate indicates a greater inability of the generation units to meet the system load demand. The calculation formula for the energy deficiency rate is as follows.

$$\zeta = \left(\sum_{t=1}^{24} P_{t,shortage}^{IES} / \sum_{t=1}^{24} P_{t,load}^{IES} \right) \times 100\% \tag{7}$$

The quantification of RE output uncertainty is used to measure the degree of deviation in the predictions of RE output, and it is a core cause of the decline in system reliability. The uncertainty of high-penetration RE output can be quantified using the following metric:

$$\sigma = \sqrt{\frac{1}{N} \sum_{t=1}^{N} (P_t^f - P_t^n)^2} \ . \tag{8}$$

The output correlation coefficient of regional RE can be used to calculate the output correlation between different RE sites and assess the spatial interconnection risks of uncertainties. The correlation coefficient of regional wind and solar outputs is defined as

$$\rho_{X,Y} = \frac{Cov(P_X, P_Y)}{\sigma_x \sigma_Y} . \tag{9}$$

2.2.2 Sensor physics data hybrid-driven dynamic fault rate perception strategy

In power systems, single-component failures threaten reliability because of significant differences in failure probabilities. Accurate failure probability models are crucial. In this study, we propose a sensor physics data hybrid-driven dynamic fault rate model, integrating equipment failure mechanisms with real-time sensor data to overcome traditional limitations and enable dynamic fault risk perception.

The construction of a time-varying and state-sensitive failure rate function is the core equation of the entire dynamic failure rate perception strategy. The formula for the time-varying and state-sensitive fault rate function is as follows.

$$\lambda(t, Z_j) = \lambda_0 \cdot g(\theta; t) \times \exp(\beta^T h(Z_j(t))) \tag{10}$$

The physical degradation term $g(\theta;t)$ in the specific implementation formula of the mechanical fatigue accumulation [Eq. (10)] is used to calculate the degree of degradation based on the fatigue accumulation degradation mechanism of mechanical components. The function $g(\theta;t)$ is typically a mechanical fatigue accumulation model, with its specific formulation given as follows.

$$\begin{cases} g(\theta;t) = \left(\dfrac{N_c(t)}{N_f} \right)^{\beta} \\ N_f = C \cdot (\Delta\sigma(t))^{-\gamma} \end{cases} \tag{11}$$

Equation (12) is a special optimization of the equipment based on Eq. (11). Gas turbines, as power generation equipment, supply electricity to the integrated energy system (IES) and provide thermal energy through cascade energy utilization. Under frequent start–stop conditions, the dynamic correction of thermal cycle damage is necessary. The fault rate function of the gas turbine thermal cycle dynamically quantifies failure risks by calculating the accumulated thermal fatigue damage from the startup and shutdown temperature differences, supporting condition-based maintenance and system scheduling optimization. On the basis of Eq. (13), the thermal cycle fatigue damage due to start–stop, $G_s(t)$, is introduced to calculate the thermal cycle failure rate function of the gas turbine. The calculation formula is as follows.

$$\lambda_r(t, Z_j) = \lambda_0 \cdot g(\theta;t) \times \exp(\beta^T h(Z_j(t))) + (1 + G_s(t)) \tag{12}$$

$$G_s(t) = \sum_{m=1}^{N_c(t)} \frac{\Delta T_m}{T_{max}} \tag{13}$$

After the dynamic fault rate perception, it is necessary to evaluate the recovery effect after the failure. We evaluate the extent of recovery of the equipment after a fault, measuring the effectiveness of repair or control measures. Active control is employed to restore the equipment to its initial state, with the recovery degree defined as

$$P(t) = 1 - \frac{\left\| Z_j(t) - Z_j(0) \right\|}{\left\| Z_{j,max} - Z_j(0) \right\|}. \tag{14}$$

On the basis of the equipment recovery level assessed from Eq. (14), whether the output capacity after the recovery of the faulty equipment meets the standards can be further determined. The unit availability is an evaluation metric that measures the system's operational capability over a specified period in the event of a single component failure, and its calculation formula is as follows.

$$\mu = \sum_{t=1}^{D_{ay}} \frac{\mathbb{I}(P_{gt} > 0)}{D_{ay}} \tag{15}$$

3. MGWO Algorithm-based Solving Method

In the optimal dispatch of the RIES, the integration of high-penetration RE introduces significant uncertainties and complexities. Testing has shown that conventional optimization methods, such as Particle Swarm Optimization and Multi-Verse Optimizer, often struggle to effectively address such high-dimensional, nonlinear, and multi-objective optimization problems. The gray wolf optimizer (GWO), which models the social hierarchy and hunting behavior of gray wolves, features a simple structure, few parameters, and high convergence speed, making it well-suited for multi-objective optimization in complex energy systems. The description of the GWO model is provided in Ref. 25.

In summary, the GWO clearly has certain limitations and drawbacks. In the original GWO, a convergence factor a decreases linearly from 2 to 0 over iterations, which does not match the algorithm's actual nonlinear convergence. To better align with this nonlinear behavior, in this paper, we propose a sinusoidal nonlinear adjustment for a, with the following formula:

$$a = a_{initial} \cdot \sin\left(\mu \cdot \frac{\pi}{2} \cdot \left(1 - \frac{l}{l_{max}}\right)\right). \tag{16}$$

By adjusting the convergence factor nonlinearly, one can effectively balance the global and local search capabilities of the algorithm. Thus, it better aligns with the nonlinear iteration process of the GWO. On this basis, we constructed a MGWO by incorporating an external archive mechanism and crowding distance sorting.

First, all nondominated solutions are identified from the initial population to form the external archive.

$$F = \left\{a \in X_o \middle| \forall b \in X_o, b \succ a\right\} \tag{17}$$

Next, the crowding distance for each solution in the nondominated front is calculated to evaluate the quality of solutions in the objective function space.

$$C_{distance}^{i} = \sum_{p=1}^{P} \frac{F_p^{max} - F_p^{min}}{Q-1} \times \frac{F_{i+1}^{p} - F_{i-1}^{p}}{F_p^{max} - F_p^{min}} \tag{18}$$

Finally, solutions are selected on the basis of their nondomination rank and crowding distance. Solutions with higher nondomination ranks are prioritized. When comparing solutions within the same nondomination rank, those with smaller crowding distances are retained.

$$O_{select}^{i} = \frac{C_{distance}^{i}}{\sum_{i=1}^{Q} (Rank_i \times C_{distance}^{i})} \tag{19}$$

The framework and pseudocode of the MGWO algorithm are illustrated in Fig. 3.

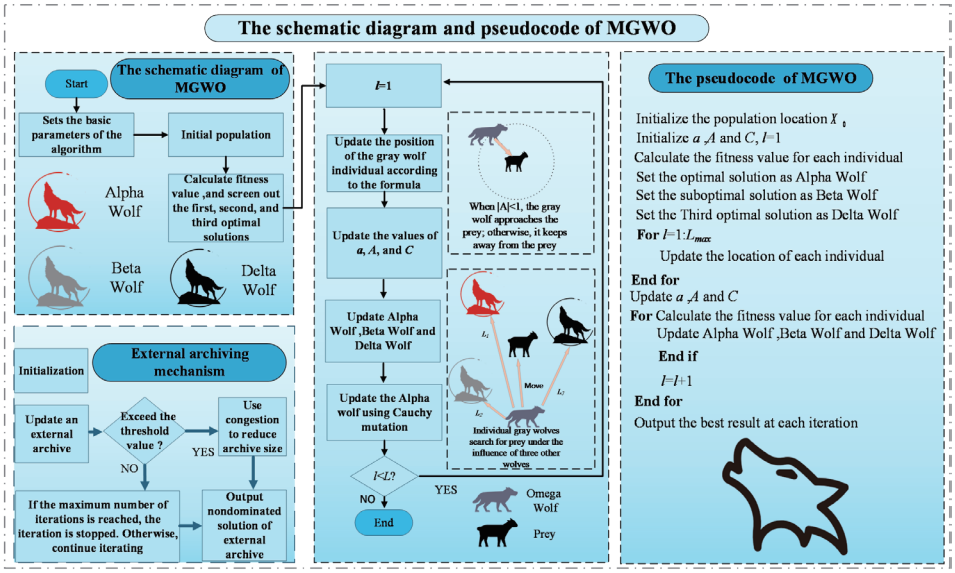

Fig. 3. (Color online) Flowchart and pseudocode of MGWO.

4. Optimization Process of Bi-level Dispatching of IES

In this study, we focused on characterizing the uncertainty of high-penetration RE output and its impact on system reliability. A physics data hybrid-driven framework is introduced for dynamic reliability assessment and risk mapping. A hybrid MGWO algorithm, inspired by the gray wolf hunting behavior, is adopted to optimize the multi-objective problem of the RIES by simulating population initialization, prey searching, and encircling strategies, while maintaining solution diversity through a repository mechanism to generate the Pareto front. The bi-level optimization scheduling of the RIES involves energy trading price setting by the energy operator (EO), internal equipment optimization in IES communities, and coordinated economic cost reduction among IESs. The energy producer (EP) optimizes its equipment output on the basis of the resulting load demand using the Gurobi solver. The MGWO algorithm adjusts EO's energy trading prices across generations by comparing objective function values. Three case studies verify the model improvements, analyzing system performance under different renewable penetration levels and equipment failure scenarios. For comprehensive details and processes, refer to Fig. 4.

5. Case Studies

To validate the proposed improved algorithm and strategies, two case studies are conducted. Case 1 validates the algorithm's superiority and versatility. Case 2 analyzes the system operation under various outputs of RE and simulates the system behavior during partial equipment failures and the subsequent recovery of the equipment to normal operation.

Figure 5 integrates two pieces of information: "power grid structure" and "multi-fuel load time series curve".

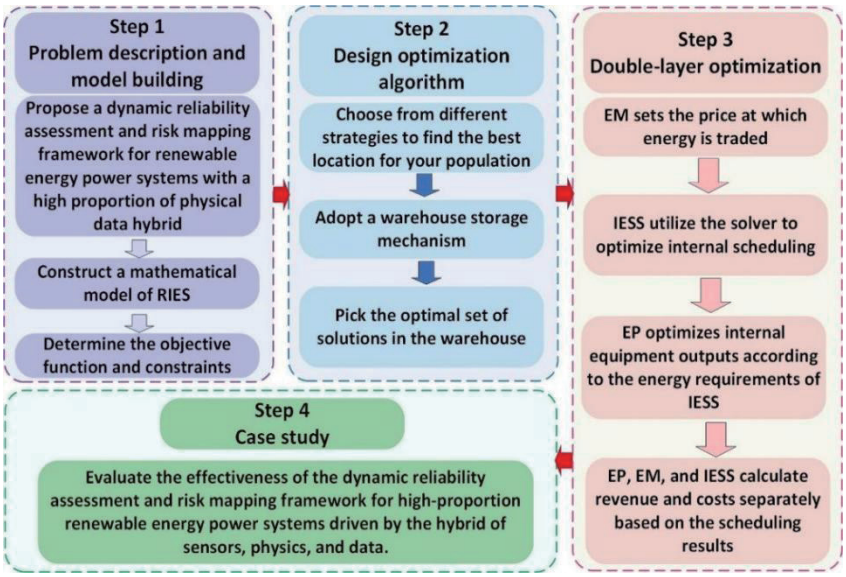

Fig. 4. (Color online) Flowchart of system optimization.

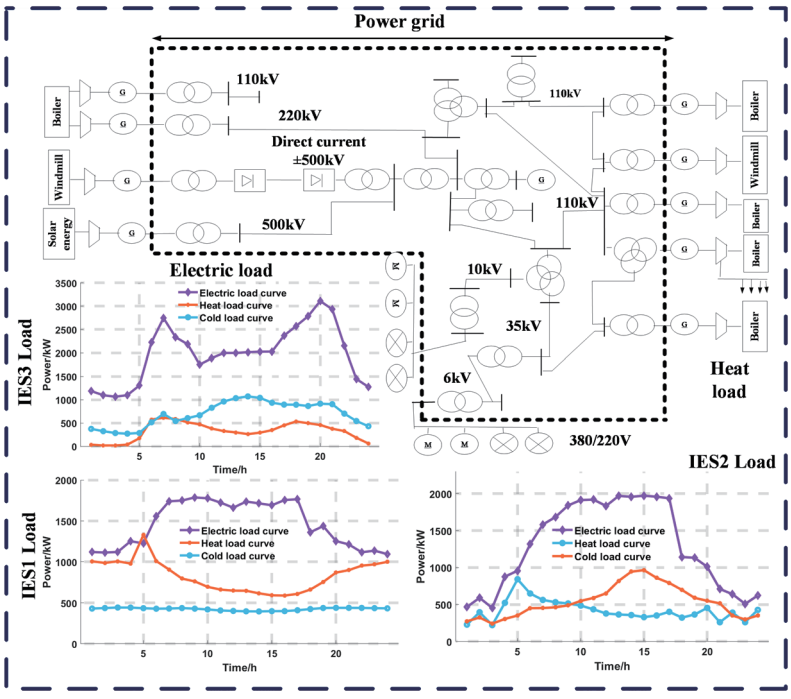

Fig. 5. (Color online) Power system structure and IES load.

In this model, the equipment failure mechanism is combined with real-time sensor data, using the measured data of deployed sensors and on the basis of the physical failure mechanism. For example, the real-time state vector of the gas turbine is derived from the measurements of the physical sensors deployed on the equipment in the pilot IES. These sensors directly monitor

operating conditions and mechanical stress parameters. The benchmark failure rate and the parameters of the physical degradation model [such as the material constants C and γ in Eq. (11)] were calibrated on the basis of the manufacturer's data tables, historical maintenance records, and accelerated life test data associated with the specific equipment model under study. The component failure scenario is introduced by the real-time state vector derived from the sensor covering a specific component, thereby triggering the dynamic failure rate model and ensuring the reliability of the model.

5.1. Case 1: Numerical and solving model validation of MGWO

To verify the versatility of the MGWO algorithm, it is integrated with system modeling and compared with Nondominated Sorting Genetic Algorithm II (NSGA-II), Termite Life Cycle Optimizer (TLCO), and GWO algorithms. Parameters are uniformly set to 50 iterations, 10 populations, and a warehouse capacity of 50 to ensure rigorous testing. Figure 6 shows the optimal solutions and iteration curves for each algorithm.

Figure 6 shows that TLCO and NSGA-II have the lowest IES costs at \$14851.2769 and \$14537.9482, but both incur losses of \$415.9558 and \$2580.1023, respectively, indicating poor system performance. GWO has a higher IES cost, but its EP revenue is \$3370.6603 higher than that of TLCO and \$4269.5130 higher than that of NSGA-II. MGWO has the lowest IES cost, reduced by 24.73, 10.93, and 9.01% compared with GWO, TLCO, and NSGA-II, respectively.

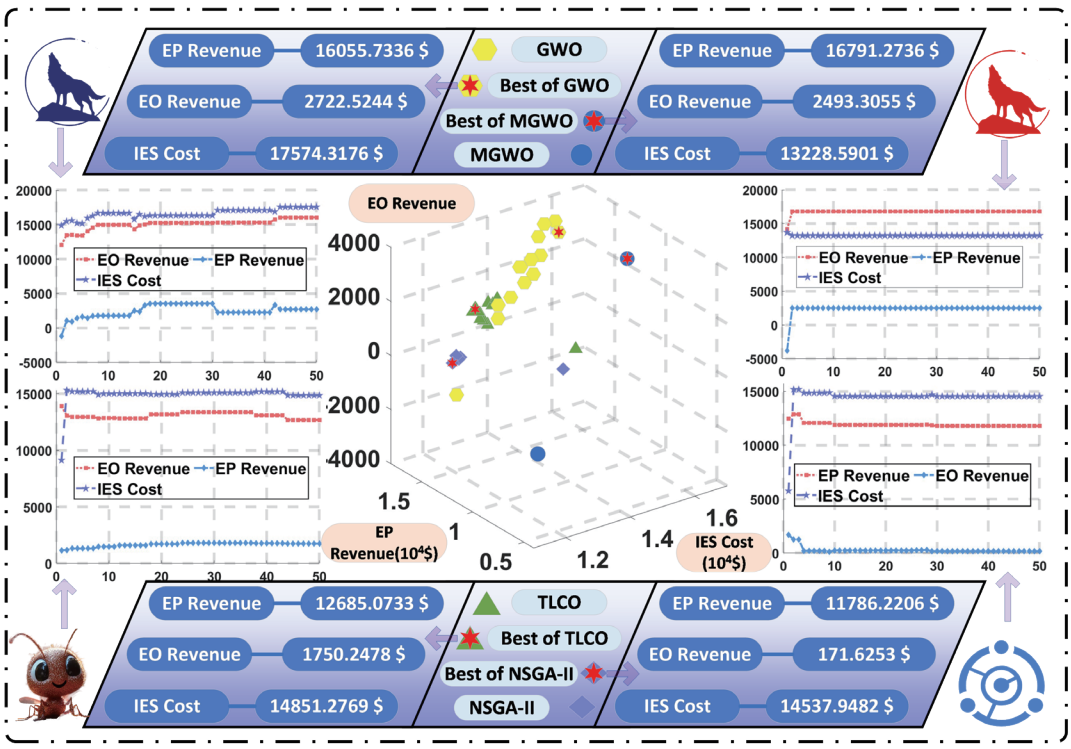

Fig. 6. (Color online) Distribution of solutions and iteration curves for each algorithm.

Although MGWO's EO revenue is slightly lower than GWO's, it is \$743.0577 higher than TLCO's and \$2321.6802 higher than NSGA-II's. MGWO's system revenue reaches \$6055.9889, a remarkable 403.01% higher than GWO's \$1203.9403. This shows that MGWO not only optimizes costs but also significantly boosts overall revenue, highlighting its versatility and competitiveness. The iteration curves also indicate that MGWO converges to the optimal solution more rapidly than the other algorithms.

5.2 Case 2: Assessment of IES performance under various new energy penetration levels and impact of single equipment failure on system operation

In Case 2, the performance of IES under different RE proportions is analyzed. Additionally, the complex impacts of gas turbine failures in IES1 and IES3 on system operation are explored. Through key indicators, the effects of gas turbine failures on operational reliability and economic performance are verified, as shown in Table 1.

In Table 1, at low renewable penetration, IES1 depends mostly on the purchased electricity (33.4%) owing to high peak demand, with wind and photovoltaic power contributing 21.2 and 32.5%, respectively, but limited energy storage discharge (4.5%). IES2 better utilizes renewables (58.6%), relying less on the grid and using energy storage discharge (15.9%) to cut costs. IES3 has the highest grid purchase share (50.2%) yet the lowest renewable utilization (29.5%), alongside insufficient energy storage.

Figure 7 shows the impact of gas turbine failures in IES1 and IES3 on system operation, including unit availability under faulty conditions, along with the corresponding output performance and power balance results.

In Fig. 7, under equipment fault conditions, IES1 and IES3 exhibit notable differences. IES1's power generation remains stable, operating between 66.7 and 87.5% utilization due to redundant design and strong fault resistance, enabling it to sell electricity to the grid at 99.27 kW (20:00) and 65.48 kW (22:00). In contrast, IES3 has a wider utilization range of 62.5–79.17% and is more reliant on external electricity during specific periods, indicating insufficient redundancy. IES3 adopts a conservative strategy to limit output fluctuations. These differences can be attributed to variations in equipment configuration, load characteristics, and control strategies.

Table 2 presents a comparison of the economic details and carbon emissions for the energy entities IESs and EP under gas turbine fault conditions ("Breakdown") and after full equipment recovery ("Recovery").

Table 1
Electricity consumption situations of different IES groups under a certain proportion of new energy integration.

IES group	Source of connected electrical energy				
	BUY (%)	PV (%)	WT (%)	GT (%)	DIS (%)
IES1	33.4	32.5	21.2	8.3	4.5
IES2	12.6	35.5	23.1	12.9	15.9
IES3	50.2	18.8	10.7	10.5	9.8

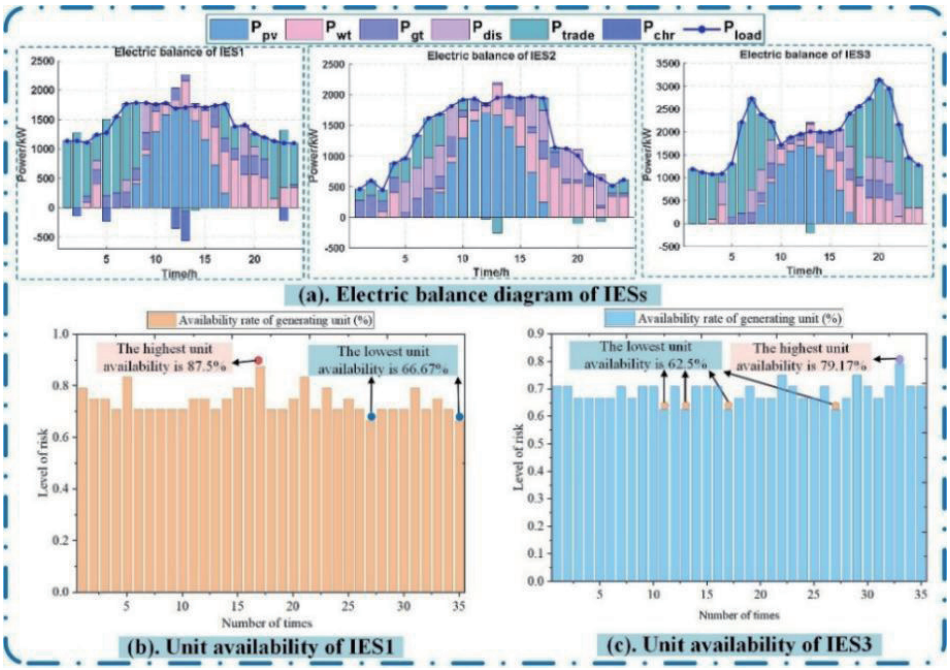

Fig. 7. (Color online) Electric balance of gas turbine and unit availability.

Table 2
Details of RIES economic composition and carbon emissions during equipment failure and after recovery.

Items		F_{eco} ($)	F_{poll} ($)	F_{om} ($)	F_{gas} ($)	Carbon (KG)
IES1	Breakdown	22031.65	449.98	744.62	4705.82	3044.34
	Recovery	20164.95	595.09	690.07	6593.21	3588.99
IES2	Breakdown	4878.12	521.38	445.11	5663.19	2930.18
	Recovery	4143.85	937.90	508.11	13299.80	4614.23
IES3	Breakdown	17984.31	446.04	1178.81	4916.84	2672.84
	Recovery	15607.15	756.80	1127.93	9538.66	4025.54
EP	Breakdown	35959.30	—	308.26	—	1469.57
	Recovery	48391.02	1691.23	955.06	23031.68	7863.67

In Table 2, during the fault period, different IES groups show how distinct fuel cost and carbon emission changes, linked to equipment, loads, and control strategies. IES3's fuel cost drops to $4916.84 owing to its energy-saving equipment configuration during partial shutdowns, but rises to $4621.82 post-recovery as energy demand increases. IES1's external energy purchases decrease by 8.5% from $22031.65 to $20164.95, possibly owing to its redundant system. Carbon emissions for IES1, IES2, and IES3 decrease by $544.65, $1684.05, and $1352.70, respectively, during the fault period. The post-recovery carbon emission surge highlights the IES groups' reliance on gas turbines to meet load demands, closely related to control strategies adjusting equipment operation modes post-recovery.

In summary, although gas turbine faults reduce fuel costs and carbon emissions in the short term, the system operates stably after recovery with optimized energy purchase costs, which is more conducive to the long-term economy of IESs.

6. Conclusions

In this study, we developed a physics data hybrid-driven dynamic reliability assessment framework to address the challenges posed by high RE penetration and component failures in power systems. Key findings are as follows:

- IES2 discharges 15.9% of its stored electricity, with 98.9% used for equipment operation and only 1.1% sold, indicating significant load demand and a need for better electricity selling strategies.
- IES3 exhibits unit availability fluctuating between 62.5 and 79.17% during failures, with a lower variability than IES1, demonstrating more stable fault response capabilities.

Innovative contributions include the following:

- a novel quantitative reliability assessment and uncertainty mapping strategy for high renewable penetration systems and
- a sensor physics data hybrid-driven dynamic fault rate perception strategy, integrating equipment physical degradation mechanisms with real-time monitoring data to construct time-varying, state-sensitive failure rate functions.

This study has limitations, such as not fully accounting for environmental impacts on RE output and focusing only on single-component failures. Future research will address the issues as follows.

- Incorporation of multi-component failure scenarios: future work will extend the current model to account for simultaneous failures of multiple components. This will involve developing advanced probabilistic failure models to assess cascading effects and system resilience under complex fault conditions.
- Integration of environmental uncertainty models: weather-dependent RE generation models will be incorporated to better capture the variability and uncertainty of solar and wind power outputs, based on environmental changes and system operating conditions, to improve forecasting accuracy and dynamic reliability assessment.
- Experimental validation in large-scale systems: The proposed framework will be tested in larger and more diverse RIESs to validate its scalability and generalizability.

These improvements aim to enhance the operational strategy for RIESs, supporting their transformation toward sustainability and reliability.

Acknowledgments

This work was supported by the project of Research and Application of Reliability Indicator System Under New Power Systems (No. YNKJXM20240586).

References

1 M. S. ElMoursi: IEEE Trans. Power Syst. **36** (2021) 563. https://doi.org/10.1109/tpwrs.2020.3041890
2 Z. F. Liu, Y. H. Huang, S. R. Zhang, X. F. Luo, X. R. Chen, J. J. Lin, Y. Tang, L. Guo, and J. X. Li: Appl. Energy **377** (2025) 124741. https://doi.org/10.1016/j.apenergy.2024.124741
3 X. L. Wang, H. Wang, B. Bhandari, and L. M. Cheng: Int. J. Precis. Eng. Manuf. Green Technol. **11** (2024) 963. https://doi.org/10.1007/s40684-023-00537-0

4 Y. Kanno: Struct. Multidiscip. Optim. **60** (2019) 83. https://doi.org/10.1007/s00158-019-02199-6
5 T. Ghanbarzadeh, D. Habibi, and A. Aziz: Renewable Sustainable Energy Rev. **212** (2025). https://doi.org/10.1016/j.rser.2025.115461
6 W. Lee, J. Woo, Y. G. Kim, and Y. Koo: Energy **310** (2024) 133194. https://doi.org/10.1016/j.energy.2024.133194
7 R. Q. Li, H. B. Ren, Q. Wu, Q. F. Li, and W. J. Gao: Renewable Energy **227** (2024) 14. https://doi.org/10.1016/j.renene.2024.120488
8 S. G. Motlagh, J. Oladigbolu, and L. Li: Appl. Energy **392** (2025) 23. https://doi.org/10.1016/j.apenergy.2025.126058
9 A. U. Rehman, J. Lu, B. Du, F. Bai, and M. J. Sanjari: Appl. Energy **393** (2025) 126147. https://doi.org/10.1016/j.apenergy.2025.126147
10 L. Sica, A. Carboni, F. Deflorio, and C. Botta: Sustainable Cities Soc. **121** (2025) 14. https://doi.org/10.1016/j.scs.2025.106175
11 M. Shariatzadeh, M. A. R. Lopes, and C. Henggeler Antunes: Appl. Energy **396** (2025) 126167. https://doi.org/10.1016/j.apenergy.2025.126167
12 B. Y. Wang, X. F. Wang, Z. W. Wang, C. X. Wei, X. P. Zhang, M. Zhou, J. W. Gao, and Z. T. Han: Appl. Energy **362** (2024) 10. https://doi.org/10.1016/j.apenergy.2024.123035
13 L. Niu, Z. Zhao, J. Tan, T. Liang, F. Zhang, N. Xiao, Y. He, S. Xie, R. Jing, J. Lin, F. Wang, and Y. Zhao: Adv. Appl. Energy **17** (2025) 100203. https://doi.org/10.1016/j.adapen.2024.100203
14 C. C. van Nooten, T. v. d. Poll, S. Füllhase, J. Heres, T. Heskes, and Y. Shapovalova: Appl. Energy **384** (2025) 125401. https://doi.org/10.1016/j.apenergy.2025.125401
15 S. Baik, J. P. Carvallo, G. L. Barbose, W. Gorman, C. Miller, and M. Spears: Int. J. Electr. Power Energy Syst. **164** (2025) 110442. https://doi.org/10.1016/j.ijepes.2024.110442
16 M. Shariatzadeh, M. A. R. Lopes, and C. Henggeler Antunes: Appl. Energy **396** (2025) 126167. https://doi.org/10.1016/j.apenergy.2025.126167
17 Y. Lu, X. Yu, X. Jin, H. Jia, and Y. Mu: IEEE Trans. Sustainable Energy. **12** (2021) 860. https://doi.org/10.1109/TSTE.2020.3023251
18 Z. Liu, Y. Pan, C. Li, S. Li, X. Yuan, and Z. Huang: J. Energy Storage **101** (2024) 113872. https://doi.org/10.1016/j.est.2024.113872
19 Q. Yang, Y. Ruan, F. Qian, H. Meng, Y. Yao, T. Xu, C. Wang, and W. Liu: Sustainable Cities Soc. **118** (2025) 106013. https://doi.org/10.1016/j.scs.2024.106013
20 A. Agarwal and T. Sharma: Renewable Sustainable Energy Rev. **215** (2025) 115620. https://doi.org/10.1016/j.rser.2025.115620
21 M. Cao, J. Guo, H. Xiao, and L. Wu: Reliab. Eng. Syst. Saf. **222** (2022) 108443. https://doi.org/10.1016/j.ress.2022.108443
22 M. Shabanian-Poodeh, R. Hooshmand, and M. Shafie-khah: Reliab. Eng. Syst. Saf. **254** (2025) 110600. https://doi.org/10.1016/j.ress.2024.110600
23 Y. Liu, R. Zheng, R. Shen, J. Zhao, Z. Shi, G. Wang, D. Yang, and Y. Li: Energy **330** (2025) 136348. https://doi.org/10.1016/j.energy.2025.136348
24 Z. F. Liu, S. X. Zhao, X. F. Luo, Y. H. Huang, R. Z. Gu, J. X. Li, and L. L. Li: Appl. Energy **379** (2025) 124918. https://doi.org/10.1016/j.apenergy.2024.124918
25 X. Yu, N. Jiang, X. Wang, and M. Li: Expert Syst. Appl. **215** (2023) 119327. https://doi.org/10.1016/j.eswa.2022.119327

Appendix of Mathematical Symbols

M_{EP}	Economic revenue of the energy producer	M_{run}	Energy producers' operating costs
M_{sell}	Income from energy sales	ε_1	Weighting factor for the respective cost components.
ε_2	Weighting factor for the respective cost components	$m^e_{t,buy}$	Real-time unit price at which the energy manager purchases electricity from producers
$E^e_{t,sell}$	Amount of electricity sold by energy producers to the energy manager	$m^h_{t,buy}$	Real-time unit price at which the energy manager purchases heat
$E^h_{t,sell}$	Amount of heat sold by energy producers to the energy manager	$m^g_{t,buy}$	Unit price at which the energy manager purchases electricity from the external grid
$E^g_{t,sell}$	Amount of electricity sold by energy producers to the external grid	$m_{t,om}$	Operation and maintenance costs of various equipment of energy producers
$m_{t,p}$	Penalty fees for pollutant emissions by energy producers	$m_{t,gas}$	Cost of natural gas purchased by energy producers
M_{EO}	Comprehensive economic revenue of the energy manager	M^e_{sell}	Economic revenue from selling electricity and heat to the IES
M^e_{buy}	Cost incurred by the energy manager when purchasing electricity and heat from energy producers	$e_{t,sell}$	Unit price at which the energy manager sells electricity to the IES
$h_{t,sell}$	Unit price at which the energy manager sells heat to the IES	$E^{IES-1}_{t,buy}$	Amount of electricity purchased by the first IES from the energy manager
$E^{IES-2}_{t,buy}$	Amount of electricity purchased by the second IES from the energy manager	$E^{IES-3}_{t,buy}$	Amount of electricity purchased by the third IES from the energy manager
$H^{IES-1}_{t,buy}$	Amount of heat purchased by the first IES from the energy manager	$H^{IES-2}_{t,buy}$	Amount of heat purchased by the second IES from the energy manager
$H^{IES-3}_{t,buy}$	Amount of heat purchased by the third IES from the energy manager	$e_{t,buy}$	Unit price at which the energy manager purchases electricity from energy producers
$h_{t,buy}$	Unit price at which the energy manager purchases heat from energy producers	$P^{IES}_{t,else}$	Output of generation units excluding photovoltaic and wind power
$P^{IES}_{t,pv}$	Photovoltaic output	$P^{IES}_{t,wt}$	Wind power output
η	Daily average reliable renewable generation capacity	ζ	Energy deficit rate
$P^{IES}_{t,shortage}$	Power deficit	$P^{IES}_{t,load}$	Load required by the IES
P^f_t	Forecasted value	P^n_t	Actual value
$\rho_{X,Y}$	Correlation coefficient of regional wind and solar	λ_j	Failure rate
λ_0	Baseline failure rate	$g(\theta;t)$	Physical degradation model
$Z_j(t)$	Real-time state vector	$h(x)$	Feature extraction function

β	Covariate weight vector	$N_c(t)$	Cumulative number of mechanical cycles
N_f	Failure cycle count under the current stress	C	Material constant
γ	Material constant	$\Delta\sigma(t)$	Real-time stress amplitude
ΔT_m	Temperature variation amplitude during the m-th start–stop cycle	T_{max}	Maximum temperature change during start–stop
$Z_j(0)$	Baseline value at the initial state	$Z_{j,max}$	Allowable limit state threshold
P_{gt}	Unit output power	D_{ay}	A 24-h period
$\mathbb{I}$	An indicator function	a	Convergence factor
$a_{initial}$	Initial value of the convergence factor	μ	Modulation coefficient
l	Current iteration number	l_{max}	Maximum number of iterations
F	Archive composed of nondominated solutions	X_o	Initial population
$b \succ a$	Solution b dominates solution a	$C^i_{distance}$	Crowding distance of solution i
P	Number of objective functions	F_p^{max}	Maximum value
$F_p^{\min}$	Minimum value	Q	Total number of solutions in the current nondominated front
F^p_{i+1}	Values of the neighboring solutions of solution i in the p-th objective function.	F^p_{i-1}	Values of the neighboring solutions of solution i in the p-th objective function.
O^i_{select}	Selection probability of solution i	$Rank_i$	Nondomination rank